Quint-Mode Square Ring Resonator and Its Applications to Various Bandpass Filters

Jinli Zhang, Haihua Chen, Ming He, Lu Ji, Xinjie Zhao, Xu Zhang

Abstract—A new type of quint-mode square ring resonator is proposed in this paper. Due to the symmetry of the resonator, the classical odd- and even-mode method is used to analyze the characteristics of the proposed resonator ,which shows that it has five resonant modes and three transmission zeros. As an example, a dual-band BPF with central frequencies (CFs) at 1.78/3.04 GHz and 3-dB fractional bandwidths (FBWs) of 10.1/18.1% is designed and fabricated. By tuning the widths of the microstrip sections, we can control the bandwidth of the second passband of the above BPF on a large scale and two single band bandwidth controllable BPFs with FBWs of 19.86% and 15.9% and CFs both at 3.5 GHz are designed and fabricated. In addition, asymmetric interdigital coupled line (AICL) is utilized to general proper couplings in these filters. What's more, the five TPs can be divided into three groups by the TZs as the lengths of the specific microstrip sections changes. Therefore, we design a dual-band BPF with good band-in-band isolation between first and second passbands, which is better than that with 26.3 dB. All of the BPFs in this paper are fabricated on the Rogers 4003C substrate with h=0.508 mm, ε_r=3.38 and tanδ=0.0027. The results of the simulation and measurement are in good agreements.

Index Terms—Quint-mode resonator (QMR), dual-band BPF, square ring resonator, bandwidth controllable, band-in-band isolation .

Ⅰ.INTRODUCTION

The Bandpass filter (BPF) is becoming a more and more essential component in modern multi-service wireless communication system. Its behaviour can influence the whole system greatly. Therefore, dual-band and wideband BPFs with high performance, such as high isolation and good passband selectivity, are undoubtedly very necessary for enhancing system functionality.

In recent years, utilizing multi-mode resonator (MMR) is the most attractive approach to design a dual-band BPF. Up to now, the dual-band BPFs developed by MMRs can be classified into two categories. The first one is using one or more stub-loaded resonators (SLRs) or stepped-impedance resonators (SIRs) to generate a dual-band BPF, such as two dual-mode SLRs in dual-band BPF[1], single quad-mode SLR in dual-band BPF[2], two dual-mode SIRs in dual-band BPF[3], and single quad-mode stub-load SIR in dual-band BPF[4]. Generally, they can reduce the size of filters and more transmission zeros are introduced to improve the passband selectivity. But the resonant modes of these resonators need appropriate coupling to build up the dual-band.

The dual-band BPFs presented in [5][6][7][8][9] belong to the second category which adopted ring resonators to excite resonate modes. In [5], a stepped-impedance ring resonator with adjustable second-passband for dual-band BPF was presented. But the condition of S-parameter need to be improved because only one transmission pole could be created in the second passband. Subsequently, the ring resonators of [6]-[9] all have four resonate modes to get desired

performance of dual-passband. Two parallel-coupled lines were placed at two nonorthogonally excited positions along a ring resonator in order to excite the two first-order degenerate modes and create multiple transmission zeros in [6]. Then, a set of perturbations is introduced on the ring to excite the two second-order degenerate modes. In [7], the two first-order degenerate modes are excited and slit for the use of the first passband by increasing the length of the loaded open-circuited stub, while one of the third-order degenerate modes moves downward and forms the second passband together with a second-order degenerate mode. Comparing with [7], two coupled-line section were installed at the two ports with 180°-separation on the square ring in [8]. In [9], a stepped-impedance ring resonator (SIRR) with two pairs of shorted stubs was proposed to design a dual-band BPF. The proposed filter not only has the controllable bandwidth and frequency space but also achieves a wide stopband.

Due to the limited degrees of freedom in the design parameter, all aformentioned filters consisted of ring resonator could not generate wide passband or regulate the bandwidth. In [10], the E-type resonators combining pseudo- interdigital coupling structure was proposed to obtain different coupling coefficients so that it could simultaneously fit the specification at each band. In [11], the bandwidths of two bands can be regulated in a range by changing the intrinsic characteristics of transversal filter and the resonator. The bandwidths of two bands of each filter could be regulated in an absolute range about 50MHz in [10] and [11].

In this work, we propose a novel quint-mode square ring resonator and establish its transmission line model. Since the resonator is symmetric, the odd- and even-mode method can be applied to analyze its resonant characteristics. Recently, some kind of quint-mode resonators (QMR) have been reported [12][13][14][15][16], but most of them were employed to design ultra-wideband (UWB) BPFs[12][14] and wideband BPFs[13][16] due to lack of transmission zeros (TZs).The proposed QMR has three TZs while the second and the third one can divide the five transmission poles (TPs) into two or three groups easily. A single wideband bandwidth controllable BPF and two dual-band BPF are designed and fabricated to demonstrate the concept above.

This paper is organized as follows. Section Ⅱ characterizes the quint-mode square ring resonator (SRR) with several graphs. Section Ⅲ presents the design procedures of A. the quint-Mode Dual-Band BPF, B. the single wideband bandwidth controllable BPFs and C. the dual-band BPF with good band-in-band isolation. Finally , in section Ⅳ, some brief conclusions are drawn for these filters .

Ⅱ.CHARATERISTICS OF SQUARE RING RESONATOR

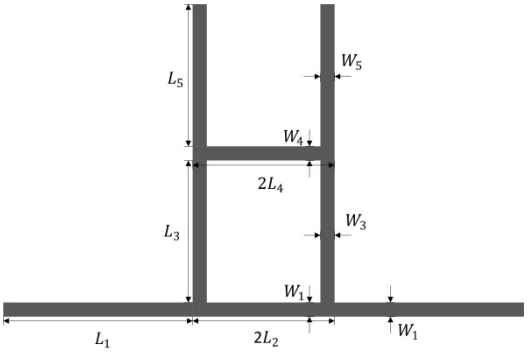

(a)

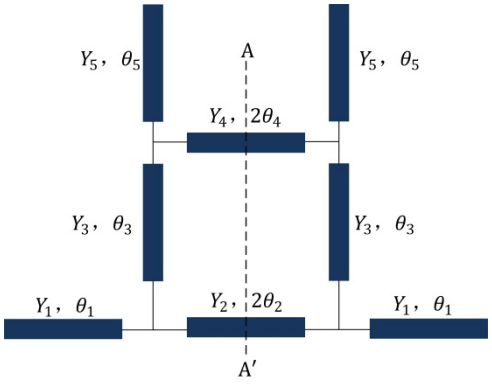

(b)

Fig.1. SRR.(a).Basic Structure.(b).Transmission Line Model

Fig.1 (a) shows the basic structure of the proposed quint-mode square ring resonator (SRR). It consists of a square ring resonator and four open microstrip lines attached to the corners of the ring. W_i and L_i (i=1, 2, 3, 4, 5) denotes the physical widths and lengths of each microstrip segment. Its transmission line model (TLM) is given in Fig.1 (b). The model is composed by eight transmission line sections and their electrical lengths and characteristic admittances are referred to θ_i and Y_i (i=1, 2, 3, 4, 5) respectively. Here, $\theta_i = \beta L_i$, where β is the propagation constant. AA' stands for the symmetric plane of the resonator.

For showing the resonator's frequency response of S21 magnitude under the weak coupling , the TLM is simulated by Agilent Technologies' simulation tool Advance Design System (ADS) 2016. As an example, θ_1 , θ_2 , θ_3 , θ_4 , θ_5 are set as 30 °, 15 °, 50 °, 5 °, 25 ° at the designed fundamental frequency f_0=1 GHz, respectively. In addition, Y_1=0.01 s and Y_2=Y_3=Y_4=Y_5=0.02 s.

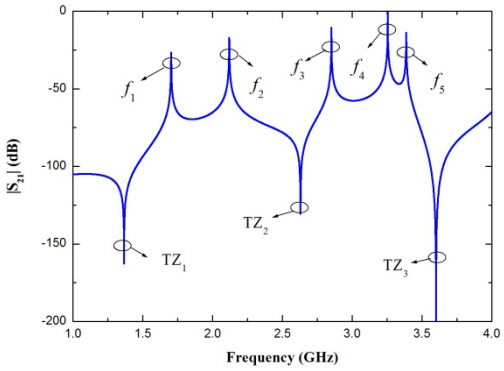

Fig.2. frequency response of S_{21} magnitude under weak coupling

From Fig.2 we can see that there are five resonant modes excited at 1.70, 2.11, 2.85, 3.25 and 3.38 GHz and three transmission zeros at 1.36, 2.63 and 3.6 GHz.

To give a deep insight into the SSR, an even- and odd-mode method is utilized. Under even- or odd-mode excitation, the symmetry plane A-A' in Fig.1 (b) can be modeled as a perfect magnetic wall (M.W.) or a prefect electric wall (E.W.). The even- and odd-mode equivalent circuits are shown in Fig.3.

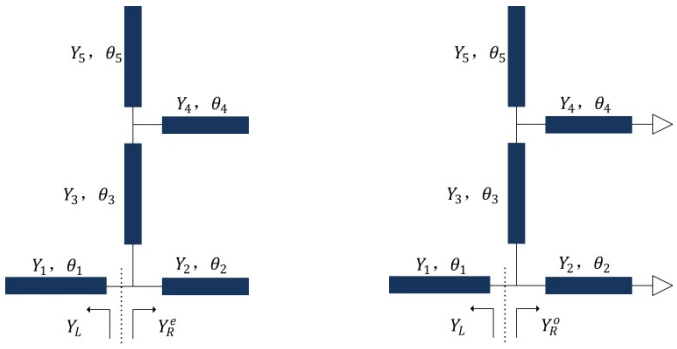

(a) (b)

Fig.3 (a) even-mode and (b) odd-mode equivalent circuits of the SSR

As illustrated in Fig.3, Y_L and $Y_R^{o,e}$ represent the two input admittances at two ports, looking into the left and right sides of the one-port bisection network. In Fig.3 (a), its resonant condition under even-mode excitation can be derived as

$$\mathrm{Im}(Y_L + Y_R^e) = 0 \tag{1}$$

where

$$Y_L = jY_1 tan\theta_1 \tag{2}$$

$$Y_R^e = jY_3 \frac{Y_4 tan\theta_4 + Y_5 tan\theta_5 + Y_3 tan\theta_3}{Y_3 - Y_4 tan\theta_3 tan\theta_4 + Y_5 tan\theta_3 tan\theta_5} + jY_2 tan\theta_2 \tag{3}$$

Similarly, as indicated in Fig.3 (a), its resonant condition under odd-mode excitation satisfy

$$\mathrm{Im}(Y_L + Y_R^o) = 0$$

where

$$Y_R^o = jY_3 \frac{-Y_4 cot\theta_4 - Y_5 cot\theta_5 + Y_3 tan\theta_3}{Y_3 + Y_4 tan\theta_3 cot\theta_4 + Y_5 tan\theta_3 cot\theta_5} - jY_2 cot\theta_2 \tag{4}$$

Substituting (2) and (3) into (1), the resonant condition under the even-mode can be deduced that

$$tan\gamma_1 \cdot \theta_1 + K_{31} \frac{K_{41} tan\gamma_1 \cdot \theta_4 + K_{51} tan\gamma_1 \cdot \theta_5 + K_{31} tan\gamma_1 \cdot \theta_3}{K_{31} - K_{41} tan\gamma_1 \cdot \theta_3 tan\gamma_1 \cdot \theta_4 + K_{51} tan\gamma_1 \cdot \theta_3 tan\gamma_1 \cdot \theta_5} + K_{21} tan\gamma_1 \cdot \theta_2 = 0 \tag{5}$$

Then, Substituting (2) and (4) into (1), the resonant condition under the odd-mode can be expressed as

$$tan\gamma_2 \cdot \theta_1 + K_{31} \frac{-K_{41} cot\gamma_2 \cdot \theta_4 - K_{51} cot\gamma_2 \cdot \theta_5 + K_{31} tan\gamma_2 \cdot \theta_3}{K_{31} + K_{41} tan\gamma_2 \cdot \theta_3 cot\gamma_2 \cdot \theta_4 + K_{51} tan\gamma_2 \cdot \theta_3 cot\gamma_2 \cdot \theta_5} - K_{21} cot\gamma_2 \cdot \theta_2 = 0 \tag{6}$$

where K_{i1} (i=2, 3, 4& 5) denotes the admittance ratio between Y_i and Y_1, and $\gamma_1 = f_{ei}/f_0$ (i=1, 2), $\gamma_2 = f_{oi}/f_0$ (i=1, 2& 3). f_{ei} and f_{oi} are the even-mode and odd-mode resonant frequencies while γ_1 and γ_2 are the normalized frequencies to f_0. By solving the roots of Eqs.(5) and (6), we can get all the two even modes and three odd modes.

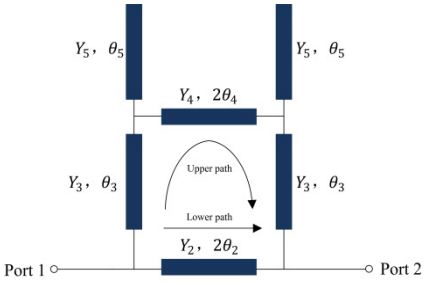

Fig.4. simplified equivalent circuit schematic with two propagation paths of SSR

There are two different propagation paths between input and output ports as shown in Fig.4. According to [17], the two signal currents excited on the input port will cancel each other on the output port. Thus, one or more TZs can be produced and calculated by following equation according to transmission line theory

$$Y_{21} = Y'_{21} + Y''_{21} = 0 \tag{7}$$

The transmission zeros can be found by solving the roots of (7).

However, it's difficult to ascertain every TP and TZ synchronously because too many parameters are in the Eq.(5) , (6) and (7) except θ_1 is fixed at 30 °. Thus, it's necessary to carry out some simulations to further understand how the inner SSR affect the TPs and TZs frequencies in ADS for speeding up design procedure.

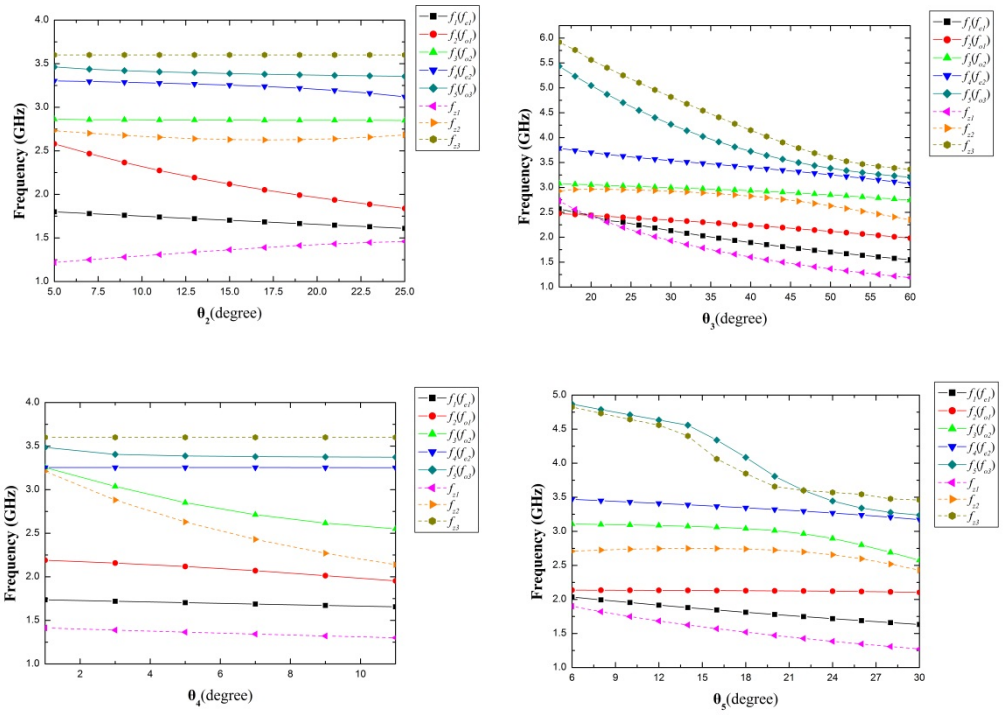

Fig.5. TP (solid line) and TZ (dash line) frequencies with varied (a) θ_2 , (b) θ_3 , (c) θ_4 and (d) θ_5

Fig.5 gives the variation of TPs and TZs versus varied θ_i (i=2, 3, 4 & 5) under the designing parameters at f_0 = 1 GHz chosen as Y_1=0.01 s and Y_2 = Y_3 = Y_4 = Y_5 = 0.02 s. In Fig.5.(a) , f_{o1} moves toward lower frequency rapidly when θ_2 increases and its same to f_{o2} and f_{z2} against θ_4 while other TPs and TZs almost not change. In addition, there is an important phenomenon shown in the Fig.5.(b). It can be observed that the relationship between f_{e1} , f_{o1} and f_{z1} is $f_{z1} < f_{e1} < f_{o1}$ when

θ_3 is larger than 20 °. And when θ_3 changes to smaller than 20 °, the relationship becomes f_{o1} <f_{e1} <f_{z1}. As illustrated in Fig.5.(d), f_{o3} and f_{z3} change relative position when θ_5 decreases from 20 ° to 10 °. In other words, three TZs can divide five TPs into two mode groups or three groups by tuning θ_3 and θ_5. We will use this property of the resonator to design a dual-band BPF with good band-in-band isolation which will be detailed in section Ⅲ.C.

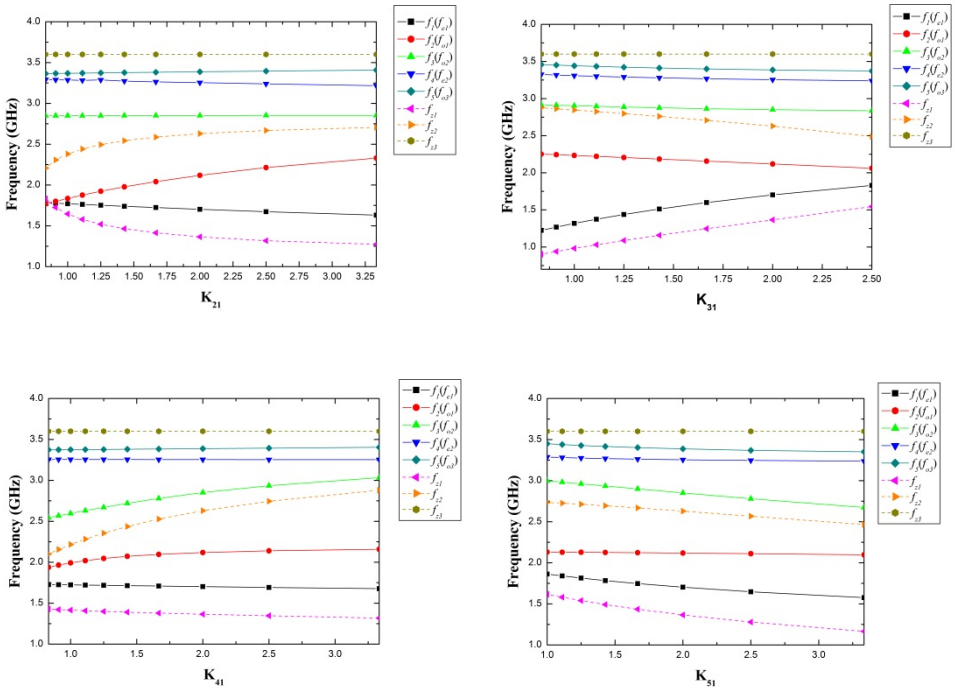

Fig.6. Variation of TP (solid line) and TZ (dash line) frequencies versus (a) K_{21} (b) K_{31} (c) K_{41} (d) K_{51}

Fig.6 plots the variation of TP and TZ frequencies versus K_{i1} (i=2, 3, 4& 5). It can be observed in Fig.6.(a) and (b) that when K_{21} increases and K_{31} decreases f_{z2} increases while the second resonant mode groups and f_{z3} are almost remain constant. Thus, K_{21} and K_{31} can be used to control f_{z2} independently to achieve sharp passband skirt without effect second passband and f_{z3}. In Fig.6 (c), f_{e2} and f_{o3} move farther away from each other slightly and the spacing between f_{o2} and f_{e2} decreases as K_{41} becomes larger. On the contrary, it can be seen in Fig.6.(d) that the increasing of K_{51} makes f_{e2} and f_{o3} move to each other nearly and separate f_{o2} and f_{e2} obviously. Therefore, the bandwidth of the second passband can be tuned by K_{41} and K_{51} easily. In Section Ⅲ.B, we present a single wideband BPF with controllable bandwidths and fabricate two BPF with absolute bandwidths 580MHz and 695MHz by utilizing different values of the widths of L_4 and L_5.

Ⅲ. BPFs DESIGN WITH PROPOSED SSR

In this section, the different θ_i (i=2, 3, 4& 5) and K_{i1} (i=2, 3, 4& 5) in SSR are applied to design quint-mode dual-band BPF, single wideband bandwidth controllable (SWBC) BPF and quad-mode dual-band BPF.

A. Quint-Mode Dual-Band BPF Design

According to the analysis in section Ⅱ, the five resonant modes can be divided into two groups by the three TZs. A quint-mode dual-band BPF is designed with the following

specifications. The center frequencies of two passbands are f_{c1}=1.76 GHz specified for FDD-LTE application and f_{c2}=3.11 GHz located in S band. The lower and higher fractional bandwidths (FBW) are Δ_1=12.4% and Δ_2=20.7%. The initial parameters are preselected $\theta_1 = 30°, \theta_2 = 15°, \theta_3 = 50°, \theta_4 = 5°, \theta_5 = 25°$ at 1GHz and $Z_1=1/Y_1$=100 Ω, $Z_i=1/Y_i$=50 Ω (i=2, 3, 4& 5) in section Ⅱ. Its physical dimensions can be calculated by using ADS LineCalc Tool, and optimized in the full-wave 3D electromagnetic (EM) simulator HFSS 15 to consider the effect of impedence discontinuities, bends and open ends by changing the lengths and the widths of each section in SSR slightly according to the analysis in section Ⅱ. Fig.7 depicts the layout of the designed quint-mode dual-band BPF. Here, asymmetric interdigital coupled line (AICL) is utilized to provide enough coupling in each passband.

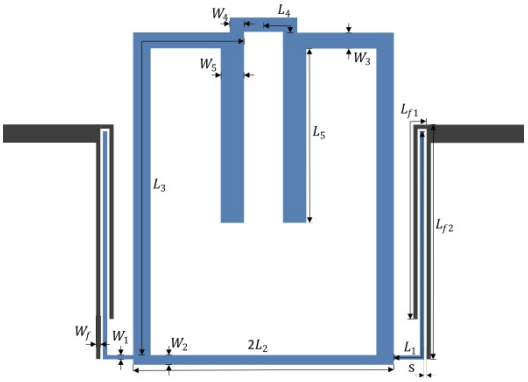

Fig.7. Layout of the designed quint-mode dual-band BPF

As studied in [18], a dual-band filter can be equivalent to the design of two single band filters independently where each passband is designed individually. Fig.8 shows the coupling scheme of the designed quint-mode dual-band BPF. f_{e1} and f_{o1} generate the first passband and f_{o2} , f_{e2} and f_{o3} generate the second passband. The lumped circuit element values of the low-pass protptype filter corresponding to the first and second passband are g_0=1, g_1=0.8431, g_2=0.622, g_3=1.3554 and g_0=1, g_1=1.0316, g_2=1.1474, g_3=1.0316, g_4=1. Then the external quality factor can be calculated by $Q_e = \frac{g_0 g_1}{FBW}$ [19] as Q_{e1}=6.79 for the first passband and Q_{e2}=4.83 for the second passband.

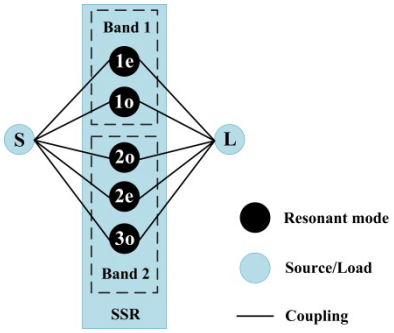

Fig. 8. Coupling scheme of Fig.7

The next step is to design the external coupling to satisfy the desired external quality factor. As shown in Fig.7, the AICL has three design degree of freedom, such as coupled length l_{f1}, l_{f2} and spacing s. The external quality factor can be characterized by

$$Q_e = \frac{f_0}{\delta f_{3-dB}}$$

where f_0 and $\delta f_{3\text{-}dB}$ represent the resonant frequency and the 3-dB bandwidth of the passband. A

full-wave simulator HFSS is used to extract the above parameters.

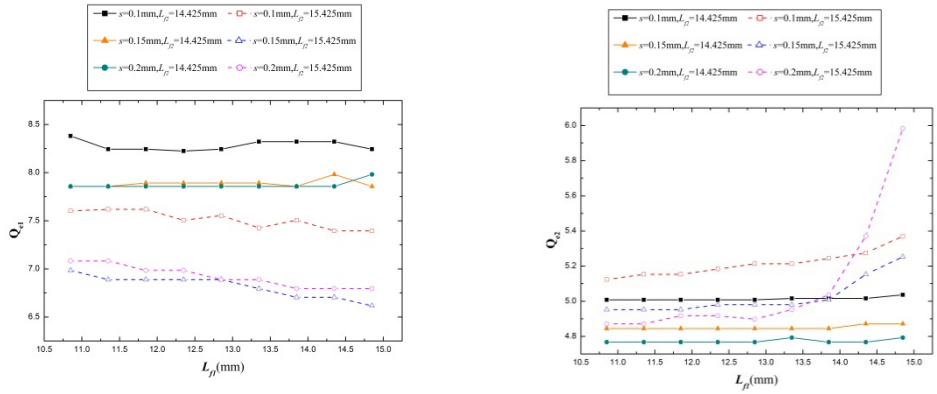

Fig.9. Extracted (a) Q_{e1} and (b) Q_{e2} versus L_{f1}

Fig.9 plots the graphs of Q_{e1} for first passband and Q_{e2} for second passband of the quint-mode dual-band BPF. In Fig.9.(a) , Q_{e1} becomes smaller as L_{f1} , L_{f2} and s increase. Similarly, it can be observed in Fig.9.(b) that Q_{e2} increases when L_{f1} ,L_{f2} increase and s narrows down. In order to meet the required Q_e for the two passbands simultaneously, there are many different combinations of the three parameters of the AICL. Here, we choose L_{f1}=13.35 mm , L_{f2}=15.12 5 mm and s=0.15 mm to design the proposed BPF.

The design procedures of the quint-mode dual-band BPF are summarized as follows.

1) The initial values of θ_i and Z_i (i=2, 3, 4& 5) are chosen to meet the required central frequency according to Fig.5 and Fig.6. Then ascertain the physical dimension of the SSR using the ADS LineCalc Tool.

2) The AICL is utilized to obtain the proper coupling of the two passbands. Finding the values of L_{f1}, L_{f2} and *s* which satisfy the requirement of the Q_e .

3) The full-wave EM simulator HFSS 15 is utilized to optimize the layout to get the final design.

Measurement is carried out using an Agilent E5071C network analyzer. The simulated and measured results of the fabricated quint-mode dual-band BPF is plotted in Fig.10 and a good agreement can be observed. And its dimensions are tabulated in Appendix. Band 1 is located at 1.78 GHz with 3-dB bandwidth of 10.1%. The measured minimum insertion loss is 1.28 dB and the return loss is 17.5 dB. Band 2 has the center frequency of 3.04 GHz and 3-dB bandwidth of 18.1%. The insertion loss is 0.7 dB and the in-band return loss is better than 18.4 dB. Three transmission zeros are generated at 1.54 GHz, 2.52 GHz and 3.64 GHz. The overall size of the filter is 22.4 mm×30.4 mm,i.e., approximately $0.24\lambda_g \times 0.33\lambda_g$, where λ_g represents the guided wavelength on the substrate at the center frequency of the first passband. The photograph of the fabricated filter is shown in Fig.11.

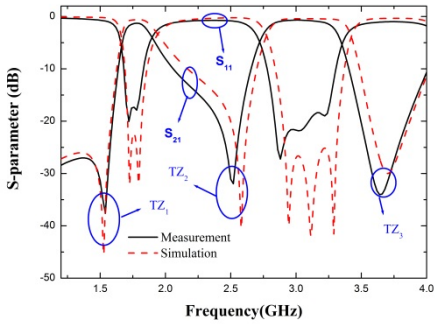

Fig.10. Simulated and measured S-parameters of the quint-mode dual-band BPF

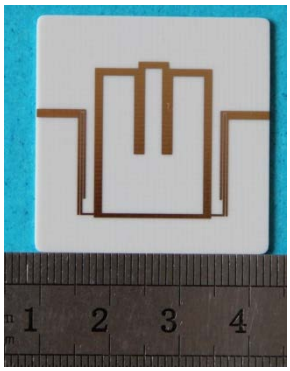

Fig.11. photograph of the quint-mode dual-band BPF

B. Single wideband bandwidth controllable BPFs Design

Before we describe the design procedure of the Single wideband bandwidth controllable BPF in detail, Δf_{35} and Δf_{45} is defined as follows:

$$\Delta f_{35}=f_{o3}-f_{o2} \qquad (8a)$$

$$\Delta f_{45}=f_{o2}-f_{e2}. \qquad (8b)$$

From Fig.6.(c),it can be seen that Δf_{45} becomes larger and Δf_{35} smaller as K_{41} increases. Similar conclusion can be drawn that when K_{51} increases Δf_{35} increases but Δf_{45} decreases. In other words, Z_4 ($1/Y_4$) and Z_5 ($1/Y_5$) can be utilized to control the bandwidth of the passband constituted by f_{o2} , f_{e2} and f_{o3} on a large scale. (For simplicity, we use the Z_i instead of Y_i and K_{i1}). Fig.12 plots the variation Δf_{35} of versus varied Z_4 and Z_5 under weak coupling while the other designing parameters preselected as θ_1=30 °, θ_2=15 °, θ_3=50 °, θ_4=5 °, θ_5=25 °, Z_1=100 Ω and Z_2=Z_3=50 Ω. With the increasing of the impedance of section L_4 and L_5, Δf_{35} becomes larger apparently .

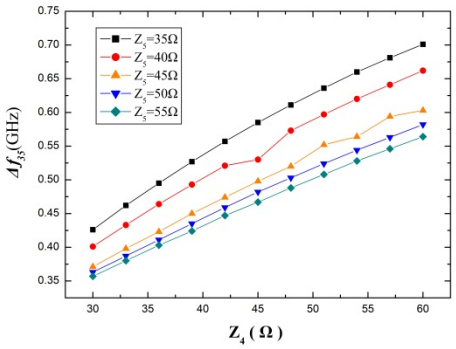

Fig.12. Variation Δf_{35} of versus varied Z_4 and Z_5 under weak coupling

To verify the conclusion aforementioned, we design two single wideband BPFs with different bandwidths by changing Z_4 and Z_5 only. The BPFs are designed with the following specifications. The center frequencies of passband is f_c=3.5 GHz specified for WiMAX application. The 3-dB fractional bandwidths (FBW) are Δ_A=21.5% and Δ_B=18.3% where subscript A denotes filter A with wider bandwidth and B denotes filter B with narrower bandwidth. The initial parameters are preselected $\theta_1 = 30°$, $\theta_2 = 15°$, $\theta_3 = 50°$, $\theta_4 = 5°$, $\theta_5 = 25°$ at 1 GHz and Z_1=1/Y_1=100Ω, Z_i=1/Y_i=50 Ω (i=2& 3). In addition, we choose Z_4=47 Ω and Z_5=55 Ω for filter A and Z_4=35 Ω and Z_5=40 Ω for filter B referring to Fig.12. After calculating the physical dimensions in ADS LineCalc Tool and optimizing them in HFSS 15, we can get the layout of proposed filters. Fig.13 depicts the layout of the designed single wideband bandwidth controllable BPFs.

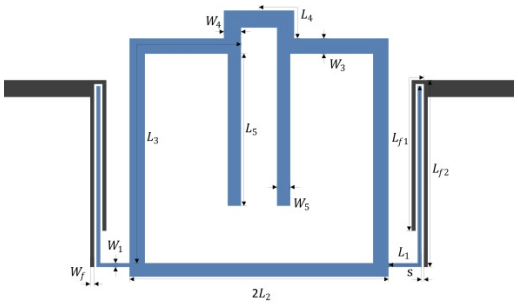

Fig.13. Layout of the designed single wideband bandwidth controllable BPFs

Being similar to the designing of the quint-mode BPF, AICL is also introduced to design the SWBC BPF. The lumped circuit element values of the low-pass prototype filter corresponding to the proposed filters are g_0=1, g_1=1.0316, g_2=1.1474, g_3=1.0316 and g_4=1. Hence, the external quality factors are calculated as Q_{eA}=4.8 for filter A and Q_{eB}=5.65 for filter B. The next step is finding the appropriate external couplings to satisfy the desired external quality factors.

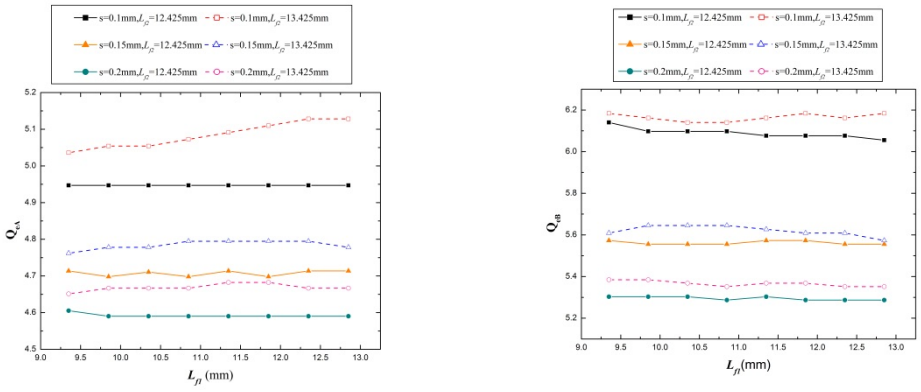

Fig.14. Extracted (a) Q_{eA} and (b) Q_{eB} versus L_{f1}

Fig.14 plots the graphs of Q_{eA} for filter A and Q_{eB} for filter B. In Fig.14.(a), Q_{eA} is almost independent of L_{f1} but increases as s and L_{f2} increase. Similarly, L_{f1} almost has no effect on Q_{eB} but Q_{eB} increases as s and L_{f2} increase. In order to meet the required Q_e for the two filters simultaneously, herein, L_{f1}=11.05 mm, L_{f2}=12.995 mm and s=0.15 mm are chosen to design the proposed BPF.

The design procedures of the SWBC BPF are summarized as follows.

1) The initial values of θ_i and Z_i (i=2, 3, 4& 5) are set to meet the required central frequency according to Fig.5, Fig.6 and Fig.12. Then ascertain the physical dimensions of the SSR using the ADS LineCalc Tool.

2) The AICL is utilized to obtain the proper coupling of the passbands of the two filters. Finding the values of L_{f1}, L_{f2} and s which satisfy the requirement of the Q_{eA} and Q_{eB}.

3) The full-wave EM simulator HFSS 15 is utilized to optimize the layout to get the final design.

Measurement is carried out using an Agilent E5071C network analyzer. The simulated and measured results of the fabricated BPFs is plotted in Fig.15 and a good agreement can be observed. Their dimensions are tabulated in Appendix. The center frequencies of the two filters are both 3.5 GHz. The measured 3-dB FBWs are Δ_A=19.86% and Δ_B=15.9%, i.e., the bandwidths of two filters can be regulated in an absolute range about 138.6 MHz. The measured minimum insertion losses and return losses are 0.6/18.82 dB for filter A and 1.3/24.26 dB for filter B. The photographs of the fabricated filters are shown in Fig.16. The overall sizes of the filters are both 22.65 mm×18.495 mm.

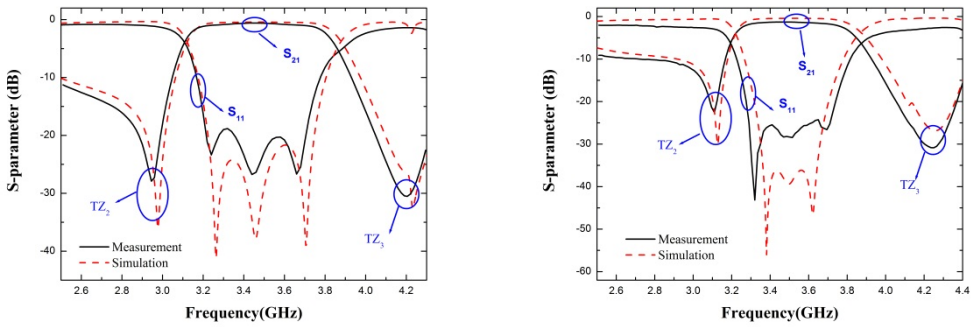

Fig.15. Simulated and measured S-parameters of (a) filter A and (b) filter B

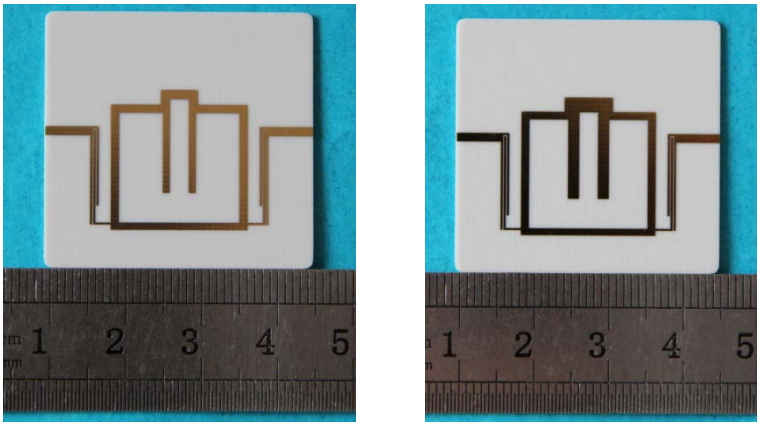

Fig.16. photograph of the (a) filter A (b) filter B

C. Dual-band BPF with good band-in-band isolation design

Further research efforts are required to explore how the lengths of L_3 and L_5 effect resonant modes distribution. Fig.17 plots the variation of TPs and TZs versus varied θ_3 with different θ_5 under the designed parameters at f_0 = 1 GHz chosen as K_{21}= K_{31}= K_{41}= K_{51}=2. In these graphs, it can be seen obviously that changing the lengths of L_3 and L_5 properly, could make the relationship between five TPs and three TZs becomes f_{e1}< f_{o2}< f_{z1}< f_{z2}<f_{o2}< f_{e2}<f_{z3}< f_{o3}. Based on this phenomenon, a dual-band BPF with good band-in-band isolation can be designed and fabricated.

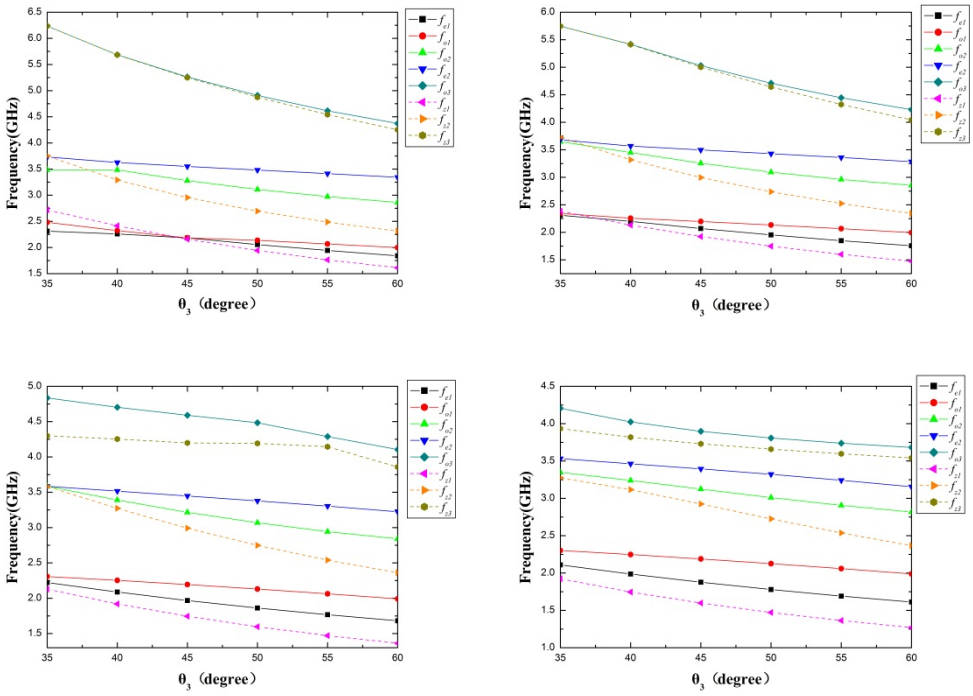

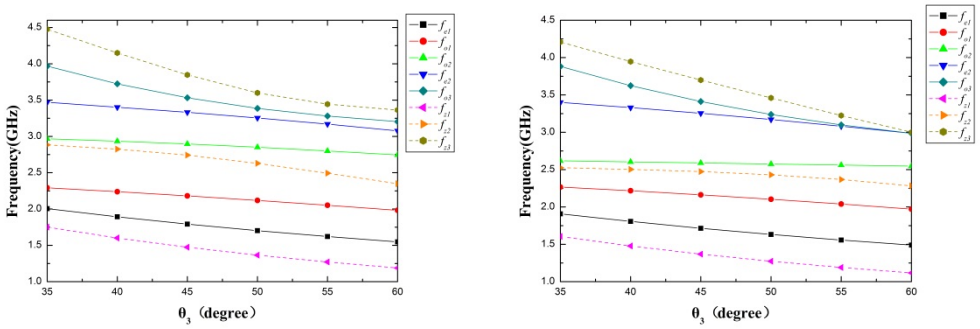

Fig.17. TP (solid line) and TZ (dash line) frequencies with (a) θ_5=5 °, (b) θ_5=10 °, (c) θ_5=15 ° , (d) θ_5=20 ° , (e) θ_5=25 ° and (f) θ_5=30 °

To demonstrate the idea, the proposed BPF is designed with the following specifications. The center frequencies of two passbands are f_{c1}=2.01 GHz specified for TD-SCDMA and f_{c2}=3.5 GHz for WiMAX. The lower and higher fractional bandwidths (FBW) are Δ_1=8% and Δ_2=8.8%. According to Fig.17 and the analysis in section Ⅱ, the initial parameters are preselected $\theta_1 = 30°$, $\theta_2 = 15°$, $\theta_3 = 40°$, $\theta_4 = 5°$, $\theta_5 = 10°$ at 1GHz. But Fig.17.(b) shows that when $\theta_3 = 40°$ and $\theta_5 = 10°$, $f_{z1} < f_{e1} < f_{o2} < f_{z2} < f_{o2} < f_{e2}$. For solving this problem, we reduce the value of K_{51}, i.e., enlarge Z_5, because other TPs and TZs are almost independent of K_{51} except f_{z1} as depict in Fig.6.(d). Therefore , Zi (i=1, 2, 3, 4& 5) are set as Z_1=70 Ω, Z_2=60 Ω, Z_3=40 Ω, Z_4=40 Ω, Z_5=70 Ω. Fig.18 shows the resonator's frequency response of S21 magnitude under the weak coupling and the S-parameters of the BPF which are simulated and optimized by ADS 2016 and HFSS 15, respectively. Fig.19 shows the layout of the designed dual-band BPF and its dimensions are tabulated in Appendix.

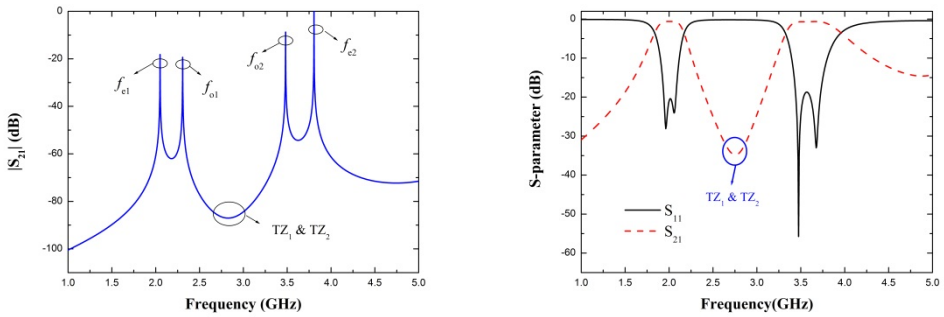

Fig.18. (a) proposed resonator's frequency response of S_{21} magnitude under weak coupling and (b) simulated S-parameters of the BPF

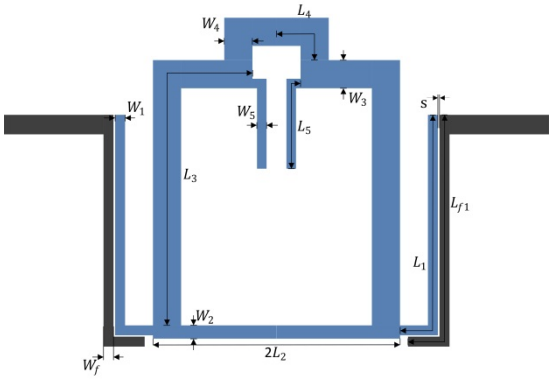

Fig19. Layout of the designed dual-band BPF

In these figures, TZ_1, TZ_2 and TZ_3 are not obvious. Referring to the analysis in Section Ⅱ, the solution we adopt is adding a microstrip segment denoted L_6 at the center of L_4. This microstrip segment can introduce a perturbation on the upper propagation path as shown in Fig.20.(a).

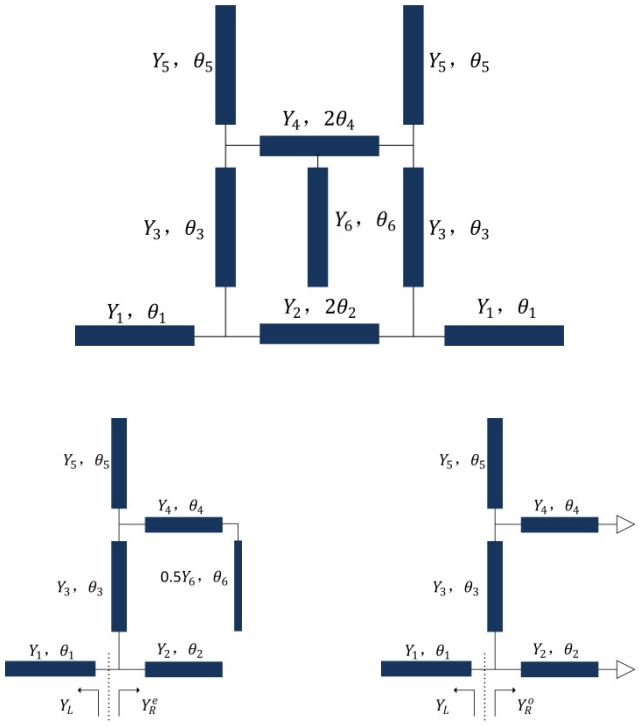

Fig20. SSR with L_6 (a) Trasmission Line Model (b) even-mode and (c) odd-mode equivalent circuits

Adding L_6 equally extends the lengths of L_4 in even-mode circuit in Fig.20.(b) and Fig.6.(c) shows that L_4 not influence the location of f_{e1} and f_{e2}. Furthermore, L_6 is shorted in odd-mode circuit and it not effect f_{o1} and f_{o2}. To validate L_6 can control f_{z1} and f_{z2} while not influence TPs, some simulations versus varied length of L_6 are carried out in HFSS 15 as illustrate in Fig.21. L_6 is introduced herein as a perturbation element in order to split f_{z1} and f_{z2}. It should be noted that f_{z3} moves to lower frequency as L_6 increases.

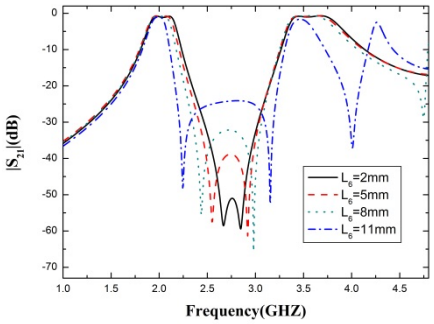

Fig21. Frequency response of S_{21} magnitude versus varied L_6

A parallel-coupled microstrip line (PCML) is applied to design the input/output coupling structure. The lumped circuit element values of the low-pass prototype filter corresponding to the proposed filters are g_0=1, g_1=0.8431, g_2=0.622, g_3=1.3554. Thus, the external quality factors are calculated as Q_{e1}=10.526 for first passband and Q_{e2}=9.615 for second passband. The following step is finding the appropriate external couplings to satisfy the desired external quality factors. The PCML has two design degrees of freedom, such as coupled length l_{f1} and spacing s in Fig.23. The final dimensions of the filter are tabulated in Appendix.

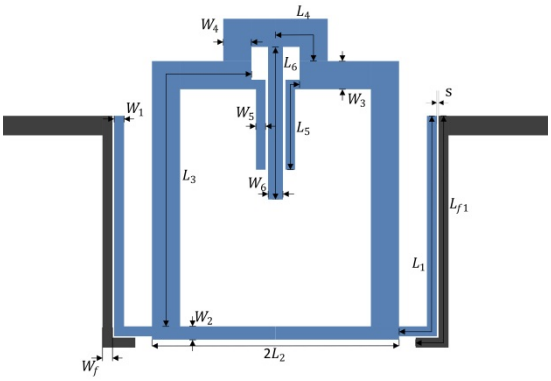

Fig.22. Layout of the proposed dual-band BPF

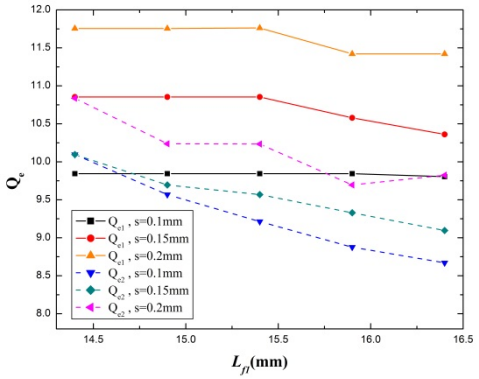

Fig.23. Extracted Q_{e1} and Q_{e2} versus L_{f1}

Fig.23 plots the graphs of Q_{e1} for first pasband and Q_{e2} for second passband. In this figure, Q_{e1} and Q_{e2} decrease as the feedline extends and s increase. In order to meet the required Q_e for the two passbands simultaneously, herein, L_{f1}=15.375 mm and s=0.15 mm are set to design the proposed BPF.

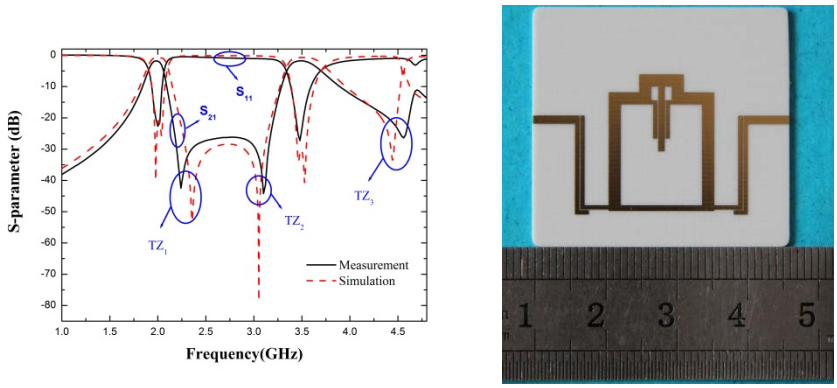

Fig.24. (a) Simulated and measured S-parameters of the filter (b) photograph of the filter

The measured dual-band central frequencies are 2.01 GHz and 3.5 GHz, while 3-dB bandwidths are 5.47% and 5.71%. And the measured insertion losses and return losses are 1.7/22.7 dB for first passband and 1.7/27.2 dB for second passband. The band-in-band isolation is better than 26.3 dB. In addition, the overall circuit size of the fabricated filter is 19.35 mm×23 mm.

Ⅳ.CONCLUSION

In this study, a novel quint-mode resonator has been proposed and was utilized to design and fabricated various filters. We can control the lacations of the TPs and TZs due to the high degrees of freedom in the design. The design procedures of all filters have been detailed to validate our idea. Predicted results was well confirmed in experiment and they exhibit several attractive features such as high return loss, good band-in-band isolation, low insertion loss and so on.

APPENDIX

	Filter A in Ⅱ.B	Filter B in Ⅱ. B	Filter in Ⅱ.C	Filter in Ⅱ.A
L_1	14.595	14.595	16.7	16.375
W_1	0.275	0.275	0.6	0.275
L_2	9.025	9.025	7.45	8.4
W_2	0.95	0.95	0.8	0.625
L_3	22.32	22.32	20.3	26.825
W_3	1.075	1.075	1.7	1.125
L_4	3.206	3.206	4	2.225
W_4	1.2	2	1.7	0.925
L_5	10.6	10.6	5.7	11.25
W_5	0.925	1.5	0.575	1.5
L_6	\	\	9.2	\
W_6	\	\	1.8	\
L_{f1}	12.955	12.955	15.425	15.125
L_{f2}	11.05	11.6	\	13.35
s	0.15	0.15	0.15	0.15

Unit : mm

REFERENCES

[1] X.-Y. Zhang, J.-X. Chen, Q. Xue and S.-M. Li, "Dual-Band bandpass filters using stub-loaded resonators," *IEEE Microw. Wireless compon. Lett.*, vol. 17, no. 8, pp. 583-585, Aug. 2007.

[2] L. Gao and X.-Y. Zhang, "High-selectivity dual-band bandpass filter using a quad-mode resonator with source-load coupling," *IEEE Microw. Wireless compon. Lett.*, vol. 23, no. 9, pp. 474-476, Sept. 2013.

[3] Q.-X. Chu and F.-C. Chen, "A Compact Dual-Band Bandpass Filter Using Meandering Stepped Impedance Resonators," *IEEE Microw. Wireless compon. Lett.*, vol. 18, no. 5, pp. 320-322, May 2008.

[4] H.-W. Liu, J.-H. Lei, Y.-L. Zhao, W.-Y. Xu, Y.-C. Fan, and T.-Y. Wu *et al.*, " Tri-band microstrip bandpass filter using dual-mode stepped-impedance resonator," *Etri Journal* , vol. 3 , no..2, pp.344-347,2013.

[5] Tsung-Hui Huang, Han-Jan Chen, Chin-Sheng Chang, Lih-Shan Chen, Yeong-Her Wang and Mau-Phon Houng, "A novel compact ring dual-mode filter with adjustable second-passband for dual-band applications," *IEEE Microw. Wireless compon. Lett.*, vol. 16, no. 6, pp. 360-362, June 2006.

[6] S. Luo, L. Zhu and S. Sun, "A dual-band ring-resonator bandpass filter based on two pairs of degenerate modes," *IEEE Trans. Microw. Theory Techn.*, vol. 58, no. 12, pp. 3427-3432, Dec. 2010.

[7] S. Sun, "A dual-band bandpass filter using a single dual-mode ring resonator," *IEEE Microw. Wireless compon. Lett.*, vol. 21, no. 6, pp. 298-300, June 2011.

[8] H.-W. Liu, B.-P. Ren, X. –H. Guan, J.-H. Lei, and S. Li, "Compact dual-band bandpass filter using quadruple-mode square ring loaded resonator (SRLR)," *IEEE Microw. Wireless compon. Lett.*, vol. 23, no. 4, pp. 181-183, April 2013.

[9] J. Shi, L. Lin, J.-X. Chen, H. Chu and X. Wu, "Dual-band bandpass filter with wide stopband using one stepped-impedance ring resonator with shorted stubs," *IEEE Microw. Wireless compon. Lett.*, vol. 24, no. 7, pp. 442-444, July 2014.

[10] M.-Q. Zhou, X.-H. Tang and F. Xiao, "Compact dual band bandpass filter using novel E-type resonators with controllable bandwidths," *IEEE Microw. Wireless compon. Lett.* , vol. 18, no. 12, pp. 779-781, Dec. 2008.

[11] M.-Q. Zhou, X.-H. Tang and F. Xiao, "Compact dual band transversal bandpass filter with multiple transmission zeros and controllable bandwidths," *IEEE Microw. Wireless compon. Lett.*, vol. 19, no. 6, pp. 347-349, June 2009.

[12] S. Sun and L. Zhu, "Wideband microstrip ring resonator bandpass filters under multiple resonances," *IEEE Trans. Microw. Theory Techn.*, vol. 55, no. 10, pp. 2176-2182, Oct. 2007.

[13] H.-W. Deng, Y.-J. Zhao, L. Zhang, X.-S. Zhang and S.-P. Gao, "Compact quintuple-mode stub-loaded resonator and UWB filter," *IEEE Microw. Wireless compon. Lett.*, vol. 20, no. 8, pp. 438-440, Aug. 2010.

[14] H.-W. Deng, Y.-J. Zhao, X.-S. Zhang, L. Zhang, and X. Lu, "Novel quintuple-mode broadband microstrip BPF with stub-loaded multiple-mode resonator, "*Microw. Opt. Techn. Lett.* ,vol.53, no.4,pp. 799–803. April 2011.

[15] F. Song, B. Wei, L. Zhu, B. Cao and X. Lu, "Dual-band high-temperature superconducting bandpass filter using quint-mode stub-loaded resonators," *IEEE Trans. Appl. Supercond.*, vol. 25, no. 4, pp. 1-10, Aug. 2015.

[16] E. G. Sahin, A. K. Gorur, C. Karpuz, and A. Gorur, "Design of UWB microstrip bandpass filter using stub-loaded quintuple-mode resonator, " *Microw. Opt. Techn. Lett.*, vol. 58, no. 3, pp. 662-666, Mar. 2016.

[17] M. Matsuo, H. Yabuki and M. Makimoto, "Dual-mode stepped-impedance ring resonator for bandpass filter applications," *IEEE Trans. Microw. Theory Techn.*, vol. 49, no. 7, pp. 1235-1240, Jul 2001.

[18] C.-F. Chen, T.-Y. Huang and R.-B. Wu, "Design of dual- and triple-passband filters using alternately cascaded multiband resonators," *IEEE Trans. Microw. Theory Techn.*, vol. 54, no. 9, pp. 3550-3558, Sept. 2006.

[19] J. S. Hong and M. J. Lancaster, *Microwave Filter for RF/Microwave Application*. New York, NY, USA: Wiley, 2011.